GDCh Research Article Angewandte International Edition Chemie www.angewandte.org

Check for updates

How to cite: *Angew. Chem. Int. Ed.* **2025**, e202510312
doi.org/10.1002/anie.202510312

Organic Materials Hot Paper

Unconventional Fast Room Temperature Synthesis of Covalent Organic Framework Single Crystals Unveiling Precise Structural Insights

Miguel Jiménez-Duro, Marcos Martínez-Fernández, Jorge J. Cabrera-Trujillo, Eva Osuna, Miguel Fernández-Ramos Humanes, Cristina Gómez-Navarro, Julio Gómez-Herrero, Félix Zamora, and José L. Segura**

Abstract: Two-dimensional covalent organic frameworks (COFs) are a special kind of crystalline polymers produced by the polycondensation reaction of organic linkers. However, the polymerization is often uncontrolled and conventionally yields polycrystalline powders. For that reason, the development of new methods to obtain single-crystalline COFs is an urgent need. Herein, we report a modulated, room-temperature, and fast synthesis of a highly fluorinated COF where the reaction conditions were systematically analyzed to yield single-crystalline rods of around three microns. The increase in crystal size enabled the analysis of precise structural features such as the mechanical properties or the different aggregation states of the bidimensional framework. In addition, the reaction mechanism was computationally elucidated, and the roles of the modulator agent and the catalyst were analyzed, confirming the critical importance of trifluoroacetic acid and 2,3,5,6-tetrafluoroaniline in modulating Schiff base bond formation and, consequently, the crystallinity of the resulting COF. This study reveals new insights into the crystallization of high-quality 2D COFs.

Introduction

Covalent organic frameworks (COFs) are a part of the mosaic comprising porous materials. These frameworks are attracting high interest owing to their unique properties, such as crystallinity or high surface area, in contrast to traditional macromolecular polymers.[1] For this reason, COFs have been introduced in a wide range of applications, including catalysis,[2] batteries,[3] or separation (and so on),[4] where the periodical arrangement of the organic matter is a key factor in establishing *structural–property* relationships. One of the most noteworthy attributes of COFs is their construction principle, which lies in the reversible reactions under thermodynamic control for the obtainment of crystalline phases following the dynamic covalent chemistry (DCC).[5] In this field, the most universal method for controlling the reversible reaction is solvothermal synthesis, which allows the reticulation process until the most thermodynamically stable structure, the crystalline phase.[6] However, several drawbacks arise from this method, where uncontrolled nucleation and growth are the most important for obtaining extended crystalline phases beyond the nanoscale. Typically, COFs are obtained as polycrystalline materials composed of agglomerated particles with domains around 100 nm.[7] Thus, the nanosized particles limit the complete characterization of structural properties of the COFs,[8] which could have key relevance for the final application beyond the study of fundamental properties, e.g. mechanical properties for membranes.[9] To improve the

[*] M. Jiménez-Duro, Dr. M. Martínez-Fernández, M. F.-R. Humanes, Prof. J. L. Segura
Departamento de Química Orgánica. Facultad de CC. Químicas, Universidad Complutense de Madrid, Madrid, Avenida Complutense s/n, Madrid 28040, Spain
E-mail: dr.marcosmartfdez@gmail.com
segura@ucm.es

Dr. J. J. Cabrera-Trujillo
Departamento de Química Orgánica, Universidad de La Laguna, Avenida Astrofísico Francisco Sánchez, s/n, La Laguna, Tenerife 38206, Spain

E. Osuna, Prof. C. Gómez-Navarro, Prof. J. Gómez-Herrero
Departamento de Física de la Materia Condensada, Universidad Autónoma de Madrid, Madrid 28049, Spain

E. Osuna, Prof. C. Gómez-Navarro, Prof. J. Gómez-Herrero, Prof. F. Zamora
Condensed Matter Physics Center (IFIMAC), Universidad Autónoma de Madrid, Madrid 28049, Spain

Prof. F. Zamora
Departamento de Química Inorgánica, Facultad de Ciencias, Universidad Autónoma de Madrid, Madrid 28049, Spain

Additional supporting information can be found online in the Supporting Information section

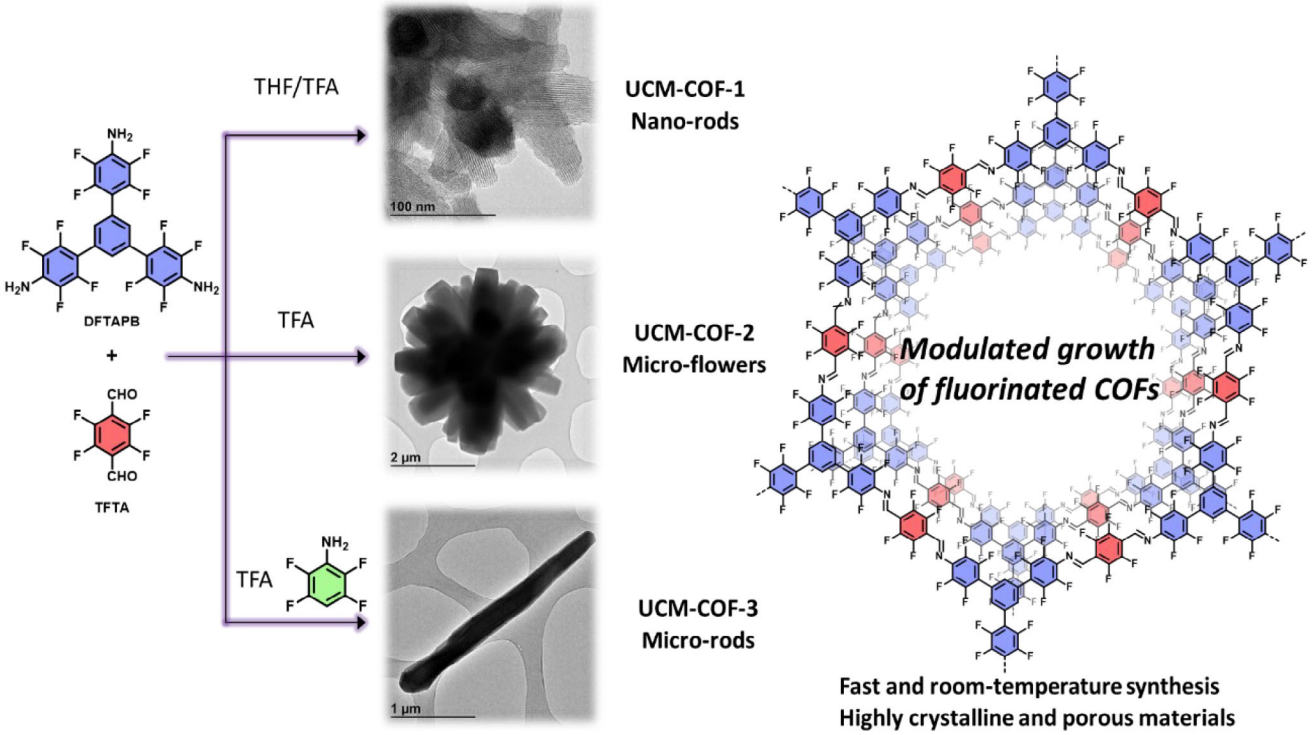

Figure 1. Schematic representation of the different DFTAPB-TFTA-COF polymorphs.

material quality, great efforts were undertaken by several groups in the past few years, and single-crystals or COFs with larger domains in the microscale (SC-COFs) are on the rise thanks to this systematic research.

The most widespread strategy to obtain SC-COFs consists of a one- to two-month reaction modulated with a monofunctional reagent, e.g. aniline for the Schiff's base reaction.[10–12] However, the long reaction time motivated the researchers to explore new protocols for the obtainment of these materials, such as seeded growth,[13] supercritical CO_2,[14] or flow-synthesis.[15] Despite the extraordinary efforts to develop SC-COFs, most of the reported methods nowadays still require complex setups or relatively high reaction times/temperatures. For these reasons, the development of SC-COFs at room temperature and open atmosphere is an area of great interest.[16] To sum up, the most widespread strategy for the synthesis of SC-COFS lies in the control of the nucleation/growth ratio to obtain the thermodynamically stable product, according to LaMer's assumptions.[17] However, the control on the equilibrium after the obtainment of the mesostructured materials to favor the isolation of SC-COFs is still unexplored.

Herein, we report the fast synthesis of three polymorphic structures of the highly fluorinated DFTAPB-TFTA-COF previously reported by our research group.[18] In this work, we modulate the synthesis of the original polymorph, named UCM-COF-1, composed of nanosized rod-like aggregates to obtain micron-sized single-crystal COF domains (Figure 1).[9] In this way, through comprehensive screening of reaction conditions, we identified the optimal crystallization parameters that produced agglomerates of flower-like COFs (UCM-COF-2) produced by an Ostwald ripening process.[19–22] Motivated for these results and taking advantage of the great reversibility conditions found, we thought that the employment of modulators should lower the nucleation/elongation processes to favor the obtainment of SC-COFs. However, we found that this strategy not only influences the morphology of the products formed but also the mechanism of its formation, observing for the first time a depolymerization stage which allows the isolation of the ≈2-3 μm SC-COFs (named UCM-COF-3, Figure 1). The obtainment of different polymorphs was demonstrated not only by X-ray diffraction but also through electronic microscopy or ^{13}C nuclear magnetic resonance. To address the robustness of the UCM-COF-3, the mechanical response of the single crystals was investigated through atomic force microscopy (AFM)-nanoindentation, revealing high fracture strength in the direction perpendicular to the c-axis. This finding aligns with previously reported high exfoliation energy values, highlighting its potential for the development of advanced materials. This work seeds new paradigms for the synthesis of SC-COFs by partial degradation of COF-based microflowers, which are more widespread morphology so far reported in literature, rather than single-crystalline COFs.

Results and Discussion

To study the COF growth dynamics, an extensive conditions screening was performed, evaluating different variables such as reaction concentration, THF/trifluoroacetic acid (TFA) ratio, temperature, and acid-catalyst. Among all the variables

a)

Proportion (THF/TFA) \ Concentration (mg/mL)	FWMH	17	35	70	140
	0/1	0.313	0.182	0.298	0.333
	0.115/0.885	0.322	0.365	0.349	0.341
	0.23/0.77	0.402	0.372	0.402	0.370
	0.5/0.5	0.370	0.430	0.410	0.499
	0.77/0.23	N.R.	N.R.	0.513	0.425

b)

Proportion (THF/TFA) \ Concentration (mg/mL)	Yield	17	35	70	140
	0/1	33	41	42	47
	0.115/0.885	70	74	75	40
	0.23/0.77	69	81	76	2
	0.5/0.5	65	77	81	12
	0.77/0.23	N.R.	N.R.	<1	<1

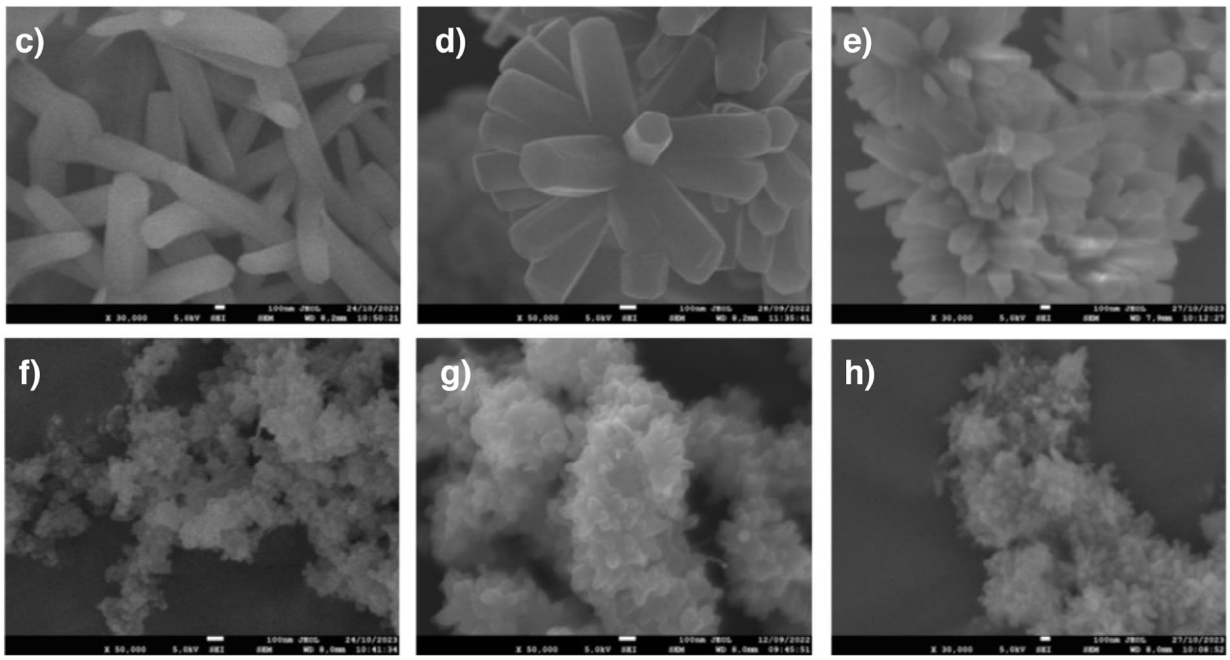

Figure 2. a) FWMH and b) yield analysis of the different conditions under study (N.R. means no reaction). Below: SEM images of the different polymorphs obtained: c) 17 mg/mL (0/1), d) 35 mg/mL (0/1), e) 70 mg/mL (0/1), f) 17 mg/mL (0.115/0.885), g) 35 mg/mL (0.115/0.885), and h) 70 mg/mL (0.115/0.885). Scale bars are 100 nm for all the micrographs. Fixed conditions: 30 °C; 24 h.

studied, the most significant changes were observed when the reaction concentration, defined as the total amount of monomers divided by the total volume of solvent, was varied along with the THF/TFA ratio (Figure 2), while keeping the temperature at 30 °C and the reaction time at 24 h constant. Thus, to identify the optimal conditions, we evaluated the full-width at medium height (FWMH) of the (100) diffraction peak from PXRD, along with the reaction yield and the morphological changes of the materials. On one hand, the reticulation processes were studied from the combination of the FWMH (Figure 2a and Figures S1-S10) and yield (Figure 2b) analysis, from it can be deduced that the amount of acid has a critical influence in the crystallization. First, most crystalline materials were obtained when pure trifluoroacetic acid was used as the reaction solvent. In addition, from the PXRD data, we could observe slight variations of the (100) maxima around 2.7° only for the mixtures containing THF, suggesting that there is a concentration dependence of the reticulation processes (e.g., ring-closing processes), unlike for the crystallizations carried out in pure TFA. This could be attributed to an enhanced kinetic constant for the COFs obtained in pure TFA, through the Arrhenius equation. Therefore, THF/TFA equilibria depend strongly on the initial monomer concentration, unlike equilibria in pure TFA, where the activation energy decreases so much that reticulation becomes more independent of the linker concentration. In good agreement, the yield of the polymerization falls by using TFA as reaction media, suggesting enhanced reversibility of the Shiff's base reaction. On the other hand, the concentration effect was clearly observed only for the mixtures using TFA as reaction media, where a proper balance between the nucleation/elongation process can be observed (FWMH, yield, and morphology). For the morphological analysis of the samples, we selected the region between 17 to 70 mg mL^{-1} of concentration and 0/1 and 0.115/0.885 of (THF/TFA) ratios (Figure 2a,b). Scanning electron microscopy (SEM)

revealed that the polymerizations carried out in pure TFA produced the largest crystals, where the concentration influenced the number of "petals" due to the increased nucleation processes, as expected (Figures 2c–h and S11-17). Despite the crystallization using a concentration of 17 mg mL^{-1} yields microflowers with fewer "petals", the FWMH value almost doubles the value of the conditions of 35 mg mL^{-1}. In this way, crystallization conditions of 0/1 (THF/TFA) and 35 mg mL^{-1} with fixed conditions of temperature (30 °C), time (24 h) were selected as optimal for this study. The microflower COFs obtained from this protocol, named as UCM-COF-2, displays a concentrical agglomeration of hexagonal prisms as expected with well-defined fringes in most of the cases. Based on these conditions, we tried to enhance the overall crystallinity of the framework by varying the temperature (5 and 60 °C), the acid employed (acetic acid and trifluoromethanesulfonic acid), and reaction time (up to 5 days). However, all the attempts to obtain bigger crystals were unsuccessful, and in all cases, the variation of the polymerization conditions yielded no reaction or did not increase the crystallinity of the samples.

To gain insights into the growth mechanism of UCM-COF-2, the evolution of the crystals was studied over time by isolating the intermediates during the polymerization. Strikingly, all the isolated products under study showed similar diffraction patterns, even at low times, such as 5 min (Figure S18). The comparison of the different diffractograms suggests that the crystallization of UCM-COF-2 is faster than expected with negligible differences in the FWMH values, achieving good crystallinities in short periods as fast as 1 h, corroborating that the pure TFA drastically lowers the activation energy of the Schiff's base formation. The intermediate frameworks were studied by SEM, revealing that the flower-like crystals grow following a typical Ostwald ripening[21] process (Figures S19-S23 and Figure 3a–c). Thus, at 5 min, we observed small particles that agree with the COF nucleation (Figures 3a and S19), while at 1 h, we registered the coexistence of this nucleus with microflowers (Figures 3b and S20), which grows by redissolution of the linkers and subsequent redeposition on the surfaces of bigger crystals.[21] Finally, for times up to 8 h, we only registered the existence of the flowers, which each one grows until ~2 μm reaching saturation at 24 h (Figures 3d and S21). In addition, the yield of the different reactions follows an exponential tendency, consistent with a nucleation–elongation process of COF growth (Figures 3d, and S19-S23).[23]

Although Ostwald ripening appears beneficial to favor the growth of large COF crystals, and the morphology of the obtained materials inhibits the obtainment of isolated microrods or "petals". Thus, based on the good results of the crystallization conditions yielding UCM-COF-2, we decided to employ different monofunctional modulators to slow the nucleation and the crystal-elongation processes. Two different modulators, with different proportions in reference to the TFTA linker were employed, aniline (H_4An) and 2,3,5,6-tetrafluoroaniline (F_4An), to analyze the possible effects of the nucleophilicity of the amines, which was recently proved to have influence in the structural properties of the final material (Tables S1 and S2).[24] On the one hand, FWMH analysis of the (100) facet revealed that the employment of F_4An maintains the crystalline features of the obtained network (Figure S24), as well as the yield of the reaction, until 10 equivs. On the other hand, if using aniline as a modulator, the FWMH values are reduced (Figure S25) with a drastic fall of the reaction yield until 2.5 equivs, suggesting a greater degree of reversibility of Schiff's base reaction. These results were confirmed by obtaining the SEM micrographs of the different materials. Strikingly, despite the great FWMH values afforded by the H_4An modulator, the morphology of the crystals still retained a flower-like morphology, and we did not find isolated crystals after examining the reaction media by electronic microscopy of the experiments with higher equivalents of aniline (Figures S26-S28). Moreover, the morphology of each petal varied from the original hexagonal-prism to less-defined crystals, indicating that the bare aniline is too nucleophile to allow the proper crystal growth. In contrast, despite the higher FWMH values afforded by the F_4An modulator, the obtainment of micron-sized single crystals was observed. First, at low modulator amounts (1 and 2.5 equivs) the morphology of the crystals varied from the microflower to spherical (dandelion-like) structures (Figures S29 and S30). Second, at medium equivalents (5 and 7.5) the microflower morphology is recovered while observing decreasing "petals" per particle in comparison with the micrographs recorded for UCM-COF-2 (Figures S31 and S32). Finally, when 10 equivs of F_4An are employed, isolated single crystals of COF (named UCM-COF-3) are successfully obtained (Figure 3e). These crystals maintain the hexagonal prism morphology that was observed for the UCM-COF-2 and can be found as individual particles, but with the difference of not forming part of bigger aggregates, microflowers. In addition, the powder X-ray diffractograms revealed the appearance of new maxima in comparison with the diffractograms recorded for UCM-COF-2 (Figure S33). Finally, upon increasing the amount of F_4An modulator, the growth of the COF was inhibited, not finding these crystals even by drop-casting the reaction media. Moreover, we attempted to explore more variables to increase the crystallite size, such as temperature or time of premixing of the modulator F_4An with the TFTA linker; however, the only variable that showed an influence on growth dynamics was the time of reaction. (vide infra).

To gain insights into the growth mechanism, we followed the reaction upon isolating the UCM-COF-3 crystals at different times. First, at 5 min we found a similar nucleus to UCM-COF-2 (by drop-casting the reaction media onto a SEM holder), but with the main difference of the observation of primal UCM-COF-3 rods (Figures 3f–h and S34). At higher times (from 1 h to 16 h), isolated single-crystals can be observed coexisting with some flower-like, but with low "petals" per particle (Figures 3g,H and S35-S39), apparently growing with the increased time. However, at around 24–30 h, only single crystals are observed (Figures S40,S41). All the materials obtained were crystalline for UCM-COF-2 (Figures S41). The plot of the yield versus time (Figure 3I) showed an unprecedented behavior, with a rapid increase up to 24 h, followed by a decrease with time, with a clear amorphization of the material, both in terms of structural features, morphological features, (Figures S42-S45) and crystallinity (Figure S46). This growth mechanism aligns well with

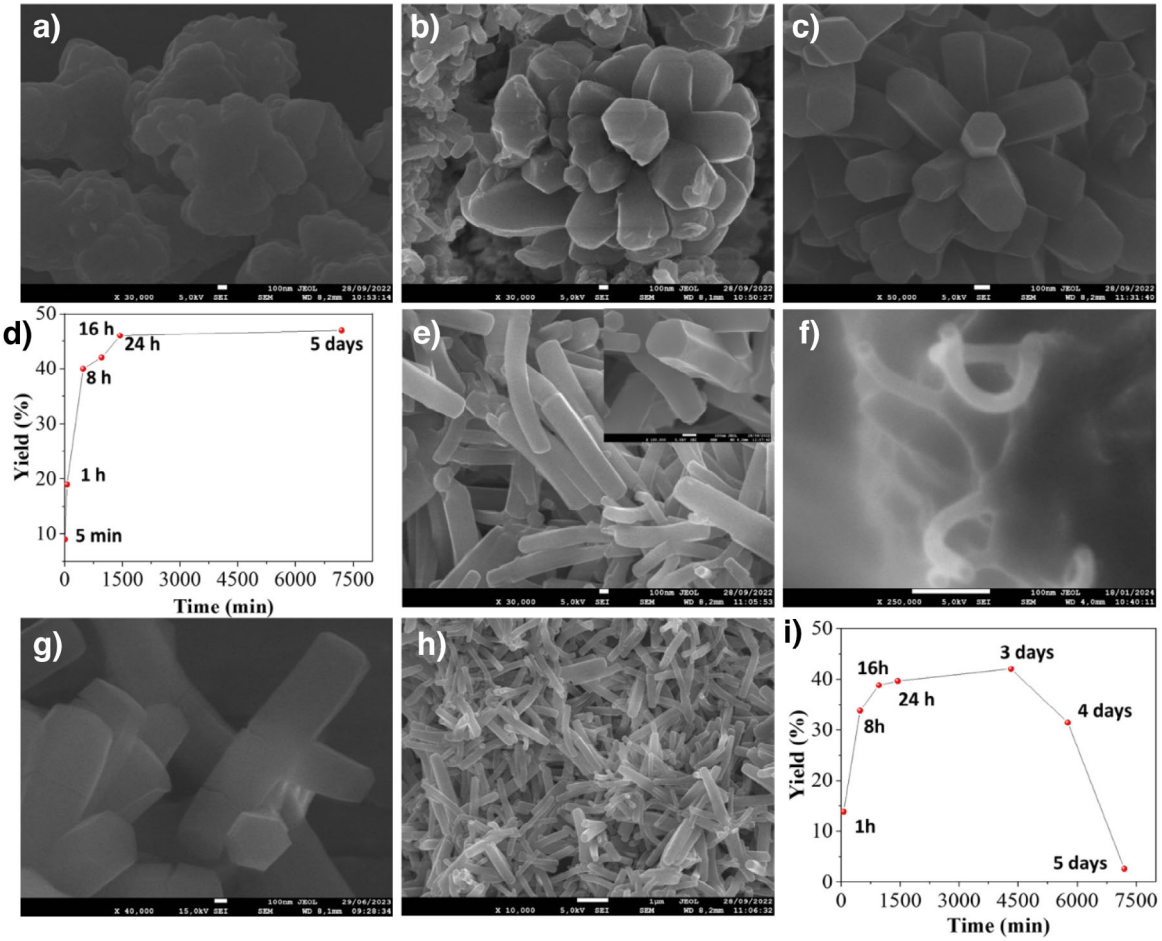

Figure 3. SEM micrographs of the Ostwald Ripening for UCM-COF-2 at a) 5 min, b) 1 h, and c) 16 h. d) Yield-time representation for UCM-COF-2. e) SEM micrographs of UCM-COF-3. Inset: magnification of a crystal showing the hexagonal shape of the crystals. Ostwald Ripening for UCM-COF-3 at f) 5 min, g) 8 h, and h) 24 h. i) Yield-time representation for UCM-COF-3.

the formation of other COF hollow structures produced by Ostwald ripening by the dissolution of the internal phase of the organic framework and favoring the organization of the external crystal. [19–22] Similarly, in this case, due to the combination of the excess F_4An modulator and the water produced during the Schiff base reaction, the obtainment of the crystals involves the evolution of the flower-like crystals by the modulation of the Ostwald ripening observed for the case of UCM-COF-2.

At first, the modulator slows down the nucleation of new particles, favoring the growth of the already-formed ones as expected.[10] However, in the second step, during the curing process, the reaction media favors the contrary reaction, first dissolving the knots joining different "petals" and, thus, allowing the obtainment of the UCM-COF-3 single-crystals. Finally, after the isolation of the single crystal, a well-defined and stable network is obtained. To better analyze the structural features of the UCM-COFs polymorphs, powder X-ray diffraction (mc-PXRD) was carried out with monochromatic Cu $K_{\alpha 1}$ radiation (Figures 4a, S47 and S48). From these data, Pawley refinements were calculated using *GSAS*-II[25,26] software to determine the crystalline structure of the different materials (Figures S49-S51). The comparison of UCM-COF-2 and UCM-COF-3 microcrystals with the nanocrystalline UCM-COF-1 diffractograms revealed a noticeable increase in the overall crystallinity of the frameworks. Thus, the (220), (310), (410), (500), (420), and (510) facets are clearly defined for UCM-COF-2 and UCM-COF-3, on the contrary for the polycrystalline UCM-COF-1. In good alignment, the FWMH of the (100) facet is narrowed from 0.420 for UCM-COF-1, to 0.193 for UCM-COF-2 and, finally, 0.103 for UCM-COF-3.

Regarding the Pawley refinements, the mc-PXRD diffractograms were refined considering P6 space group symmetry of hexagonal system for the unit cell, where the fluorinated COF layers are stacked in an eclipsed (AA) disposition along the *c*-axis.[18] These refinements adjusted well to the diffraction profiles according to the refinement parameters (R_w, χ, R, and R_{bkg}), especially for UCM-COF-2 and UCM-COF-3 (Table S3). Despite the refined *c*-axis length being different in UCM-COF-3 than the others, the experimental patterns fit well with the simulated ones for the AA-stacked unit cell, unlike for the AB-stacked one, especially above 8° (Figures S52-S55), indicating the great quality of the obtained phases. This can be explained by the fact that the microrod morphology of this sample makes powder x-ray diffraction not the most suitable technique to determine the crystalline structure as

the particles appear to consist of single crystals. Around 25° in 2θ units, a wide diffraction maximum appears in all measurements, which represents π-π stacking. In UCM-COF-1 this peak appears with lower intensity because of the higher polycrystallinity of the sample as they present a nanorod morphology. On the other hand, this maximum increases in intensity and becomes more defined in UCM-COF-2, which is also a polycrystalline sample but with a larger particle size. However, this is not observed for UCM-COF-3, where a higher intensity and definition would, therefore, be expected for this maximum. This could be rationalized due to the preferential disposition of the particles in the samples: UCM-COF-2 particles are formed by several microrods oriented in all directions, which are joined by a knot, while UCM-COF-3 microrods have a preferential orientation, where the *c*-axis is perpendicular to the vertical axis. The characterization was complemented with transmission electron microscopy (TEM), where highly ordered crystallographic planes were observed at high magnifications for all the UCM-COFs (Figures S56-S63). Moreover, the particles observed for UCM-COF-2 (Figures S57-59) and UCM-COF-3 (Figures S60-S63) were clearly more ordered than the particles observed for UCM-COF-1, in good correlation with the PXRD experiments. Interestingly, the crystals obtained for UCM-COF-3 ends in corrugated morphology, which aligns with the growth mechanism mentioned above. In addition, these crystals show slight flexibility without losing the long-range ordering, as can be observed for the TEM micrographs at higher magnifications (Figures S62 and S63). Furthermore, we could observe the existence of structural defects for UCM-COF-3 (Figures S63-66), not observed for UCM-COF-2 (Figures S58,S59), probably produced by the modulation of the Ostwald ripening process as stated above. Thanks to the single-crystal structure of UCM-COF-3 and in order to deepen the study of this polymorph, high-resolution transmission electron microscopy (HR-TEM) equipped with a goniometer was used to analyze the preferential orientation of this framework (Figure 4), allowing us to better observe the structural order of this material, both along the prism and its hexagonal faces (Figures 4a,d and S67- S73). With the HR-TEM micrographs, a Fourier transform (FT) analysis was carried out over these observed planes (Figure 4b,e) to simulate electron diffraction (ED) patterns and determine which crystallographic planes were observed. The pattern with [001] zone axis is characteristic of a hexagonal crystalline structure,[27] as predicted in the Pawley refinements. Also, thanks to image processing techniques with *ImageJ* software,[28] the interplanar distances were calculated. The obtained distances have values of 2.6 and 1.96 nm and correspond respectively to (100) and (110) planes, where the first one also aligns with the pore diameter (Figure 4c,f).

Next, we performed density functional theory (DFT) calculations to explore the mechanism behind Schiff base formation. Particular attention was given to how trifluoroacetic acid (TFA) and the modulator F_4An influence the crystallinity of the resulting covalent organic framework (COF). First, we computed the direct TFA-catalyzed reaction between the dialdehyde TFTA and the triamine DFTAPB, without any modulator present (Figure 5, green pathway). The reaction is initiated by the TFA-assisted amine addition to the aldehyde (TS1) with a calculated activation barrier of 9.2 kcal mol^{-1}, leading to the formation of the hemiaminal intermediate in a nearly thermoneutral process (INT1: −0.5 kcal mol^{-1}). Our calculations reveal that TFA plays a crucial dual role in this step: it increases the electrophilicity of the aldehyde by forming a hydrogen bond with the carbonyl group, while simultaneously acting as a proton acceptor through its oxo group, enhancing the nucleophilicity of the attacking amine. Subsequently, the rate-determining step (RDS) occurs via TS2, corresponding to the TFA-assisted dehydration, with an activation barrier of 15.5 kcal mol^{-1}. Although higher than TS1, this barrier remains consistent with a rapid reaction at room temperature. The assignment of TS2 as the RDS aligns with previously reported computational studies on Schiff base formation.[29–31] Notably, in this TS2, TFA again plays a significant dual role: it deprotonates the hemiaminal via its oxo group while simultaneously protonating the hydroxyl group, facilitating a water molecule release. The reaction then yields the imine intermediate INT2 in an overall slightly endergonic process (+2.1 kcal mol^{-1}).

In order to compare this direct reaction, we next examined the analogous mechanism involving the modulator F_4An, followed by an imine exchange process (Figure 5, black and blue pathways, respectively). Interestingly, we found only minor energetic and geometric differences between the pathway involving F_4An and the direct reaction with DFTAPB. For TS1, INT1, TS2, and INT2, all energetic differences lie within a narrow range of less than 0.5 kcal mol^{-1}. A detailed geometrical comparison of these species is presented in Figure S74.

Finally, we examined the imine exchange reaction where the initial formed imine from TFTA and the modulator F_4An undergo substitution by the triamine DFTAPB. This process starts with the DFTAPB attacking the imine through TS3 with a computed barrier of 19.1 kcal mol^{-1}. As expected, due to the lower electrophilicity of imines compared to aldehydes, TS3 is higher in energy than the corresponding amine addition to the aldehyde (TS1), which translates to a much slower addition process. TS3 is also higher in energy than the rate-determining step for the process without modulator (TS2). In the last step of the reaction mechanism, the modulator is regenerated via TS4. Unlike the reaction without F_4An, here TS4 is isoenergetic with amine addition ($\Delta G^{\ddagger}$ (TS3) = $\Delta G^{\ddagger}$ (TS4) = 19.1 kcal mol^{-1}) and the overall process is slightly exothermic (ΔG = -3.7 kcal mol^{-1}). We propose that the overall activation barriers for the first and second processes (15.5 and 19.1 kcal mol^{-1}, without and with modulator, respectively) reflect differences in the kinetics of bond formation that may influence network assembly. In particular, the higher barrier for the second process suggests slower framework evolution, which could allow for enhanced structural reorganization during growth and potentially contribute to the improved crystallinity observed when F_4An is used as a modulator.[11]

The organic composition of the UCM-COFs was studied by Fourier-transformed infrared (FTIR) and ^{13}C cross-polarization magic-angle-spinning nuclear magnetic resonance, ^{13}C-CP-MAS-NMR, and spectroscopies. On the one hand, FTIR spectra of UCM-COF-1 and UCM-COF-2

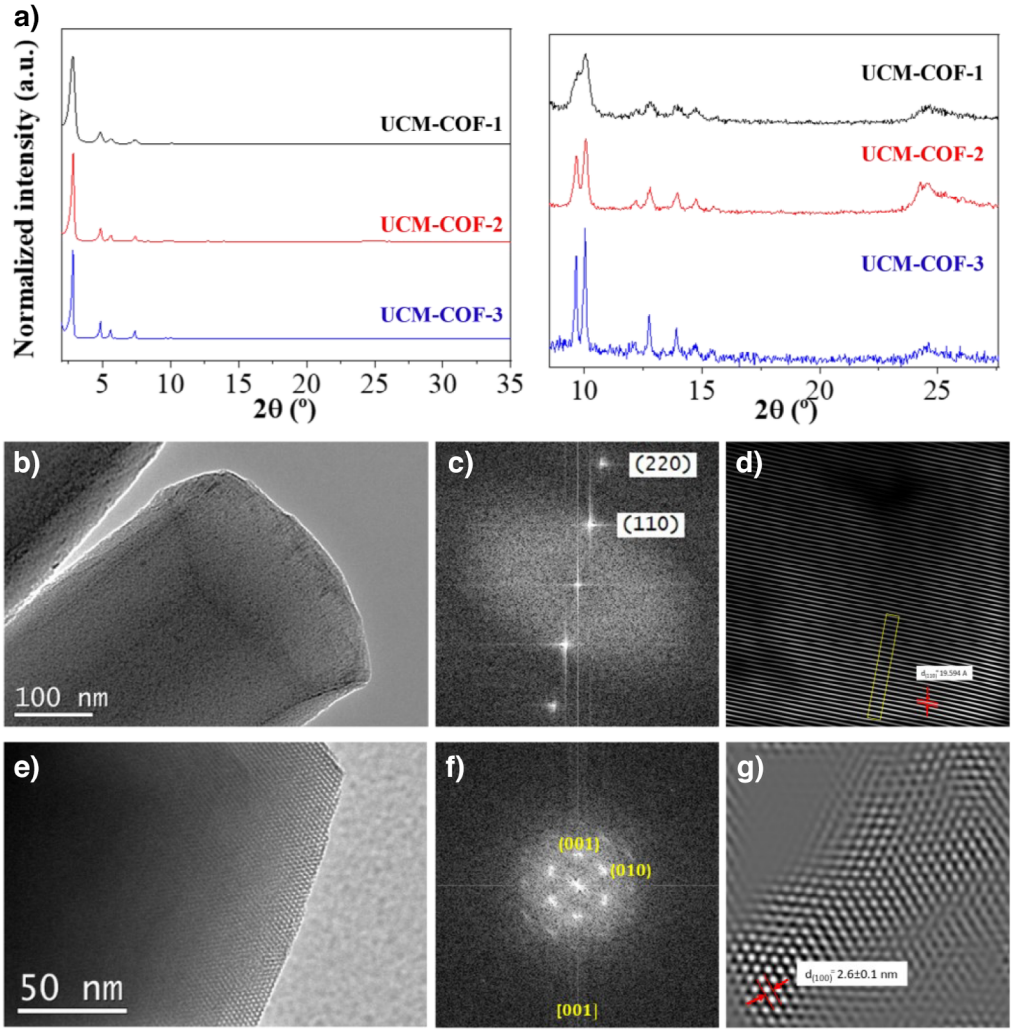

Figure 4. a) mc PXRD of the different UCM-COFs. b) Side-look of the HR-TEM micrograph obtained for UCM-COF-3. c) SAED pattern obtained by FTT of the side-look of UCM-COF-3. d) Reconstructed image of the side-look of UCM-COF-3. e) Top-look of the HR-TEM micrograph obtained for UCM-COF-3. f) SAED pattern obtained by FTT of the top look of UCM-COF-3. g) Reconstructed image of the top look of UCM-COF-3.

showed the fading of the amine N-H (*ca.* 3400–3200 cm^{-1}) and aldehyde C=O (*ca.* 1685 cm^{-1}) stretching, as expected for a complete polymerization. However, FTIR of UCM-COF-3still shows remanent terminal aldehydes, probably due to the modulation of the F_4An. In addition, the imine sorption band appears at 1622 cm^{-1} for all the products, and the three spectra show negligible variations in the relative intensities or band displacement for all the absorptions in the different materials (Figure S75). On the other hand, the ^{13}C-CP-MAS-NMR spectra of the UCM-COFs revealed the appearance of an imine signal at ca. 158 ppm with the absence of the aldehyde signal at around 180 ppm, confirming the successful of the polymerization in all the cases (Figure 6a). Moreover, interesting differences according to the different degrees of crystallinity of the polymorphs can be observed in the ^{13}C-CP-MAS-NMR spectra. Thus, for UCM-COF-2 and UCM-COF-3 the spectra present better defined signals in contrast with those found for UCM-COF-1. It is worth mentioning that ^{13}C-CP-MAS-NMR has already been used for the study of the COF structures. However, these studies compared different COFs, only being able to quantify the AA stacking from the nonAA stacking regions in the COFs, despite the good crystallinities of the materials evaluated.[32] It should be noticed that despite these three polymorphs built up from the same organic linkers conforming frameworks with identical unit cells, the chemical environment of every anisochronous nuclei is different depending on the degree of crystallinity of the framework. In this way, beyond the degree of AA stacking, depending on the crystallite size, the chemical environment of the ^{13}C isotopes could vary as a function of the proximity of the surface of the particle, as well as to the inner shell of the grain. This could be rationalized in terms of the increased electronic density surrounding the carbon nuclei with the enhanced number of stacked layers, which shields the isotope from the magnetic field, and thus, the signals corresponding to bigger crystals appear at higher fields. On the contrary, if the nuclei are part of the atoms conforming to the surface, the signals appear unshielded. By comparison of the solution ^{13}C-NMR spectra of the TFTA (aldehyde) and the DFTAPB (amine) linkers with the ^{13}C-CP-MAS-NMR

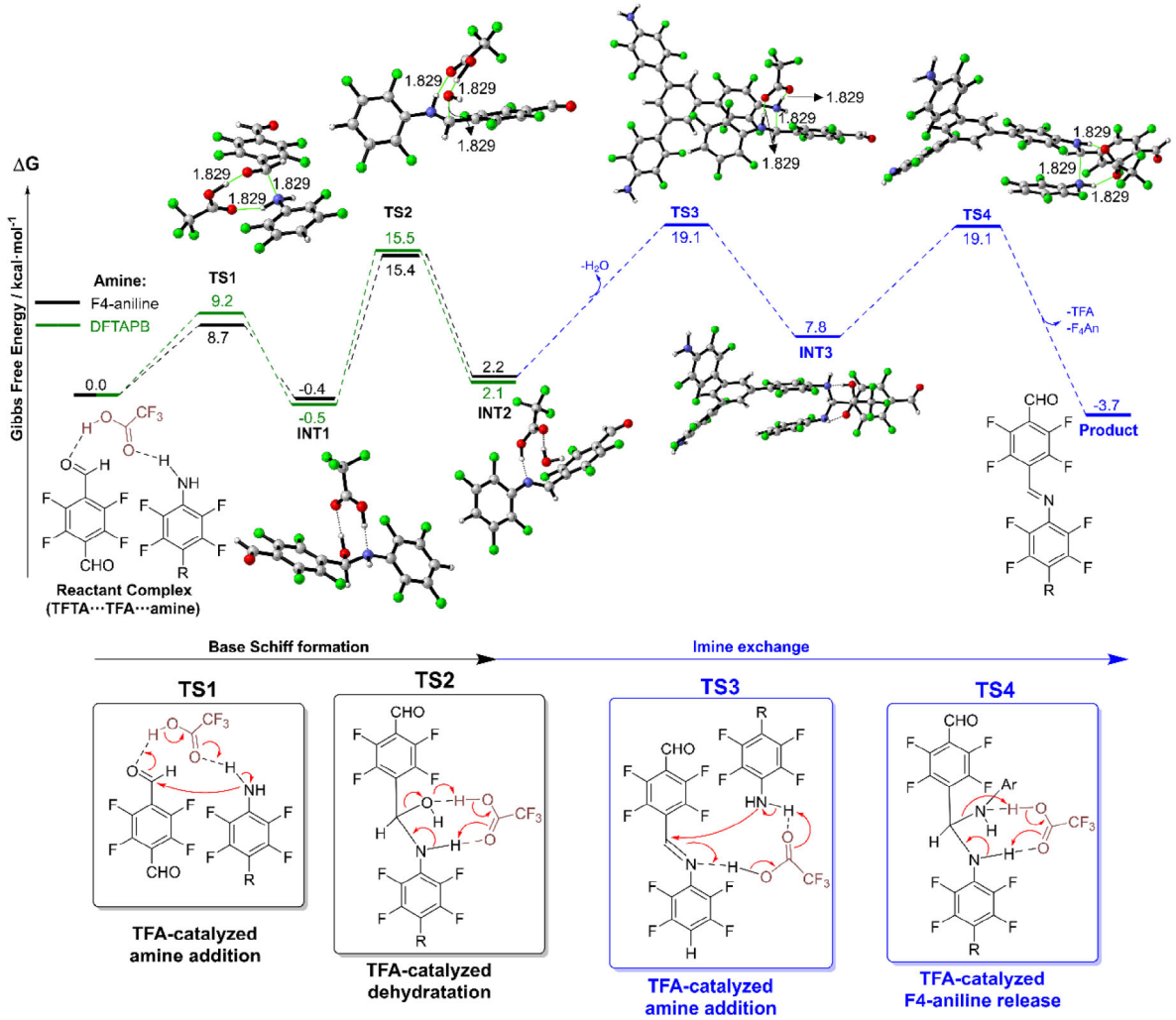

Figure 5. Reaction profiles for the TFA-catalyzed reaction of TFTA with DFTAPB (green pathway) and comparison with the same TFA-catalyzed reaction using F_4An as modulator (black pathway), followed with an imine exchange with DFTAPB (Blue pathway). All energy values are given in kcal mol^{-1} and all data have been computed at the level of theory denoted as PCM(THF)-M06-2X/def2-TZVP//PCM(THF)-M06-2X/def2-SVP. For clarity, in the base Schiff formation, only structures involving the F_4An modulator are shown.

spectra of the COFs we could see that all the signals fall in the aromatic region, while the signals corresponding to the imine linkages appear unshielded without interfering with the rest of the nuclei (Figures S76-S78). Therefore, following the protocol reported by Kang et al.[32] for this COF, the imine signal can be used as a probe to study the aggregation of the different UCM-COFs (Figure 6b). The signal corresponding to UCM-COF-1 displays four main contributions at ca. 161, 159, 156, and 155 ppm, labelled from 1 to 4 in that order, representing the 13%, 64% 22%, and 1% of its area calculated by Gaussian deconvolution. On contrary, for UCM-COF-2 and UCM-COF-3, the calculated area of the contribution 1 disappears due to the more intimate interaction between the layers and to the higher degree of crystallinity of these samples. In other words, UCM-COF-1 presents more surface area of the COF particles due to the smaller size of the rod-like particles of this polymorph, exposing more ^{13}C isotopes to the magnetic field appearing unshielded (contribution 1). Thus, for UCM-COF-2 the contributions are 11% for 2, 72% for 3, and 18% for 4, meanwhile, for UCM-COF-3 0%, 11%, 89%, and 10%, respectively. These results suggest that the nucleus of the surfaces mainly produces contributions 1 and 2, while contributions 3 and 4 correspond to the ones conforming the interior of the crystals. In addition, we hypothesize that signal 4 represents the inner shell of the crystallites, where its contribution for UCM-COF-2 is greater than for UCM-COF-3 due to the existence of the knots joining the "petals" of the flower-like microcrystals. On the basis of this analysis, we could corroborate that the UCM-COF-3 presents the more significant AA-staking domains with the most regular shape of the crystals in good alignment with the observations found in XRD and microscopy. The effect of the particle size and morphology of the aforementioned COFs was also evaluated through ^{19}F-CP-MAS-NMR spectroscopy. First, we compared the obtained spectra with the ^{19}F-NMR solution spectra of the amine and the aldehyde. As can be seen in Figures S79-81, there is a slight variation in the chemical shift between the COFs and the signals of the free monomers.

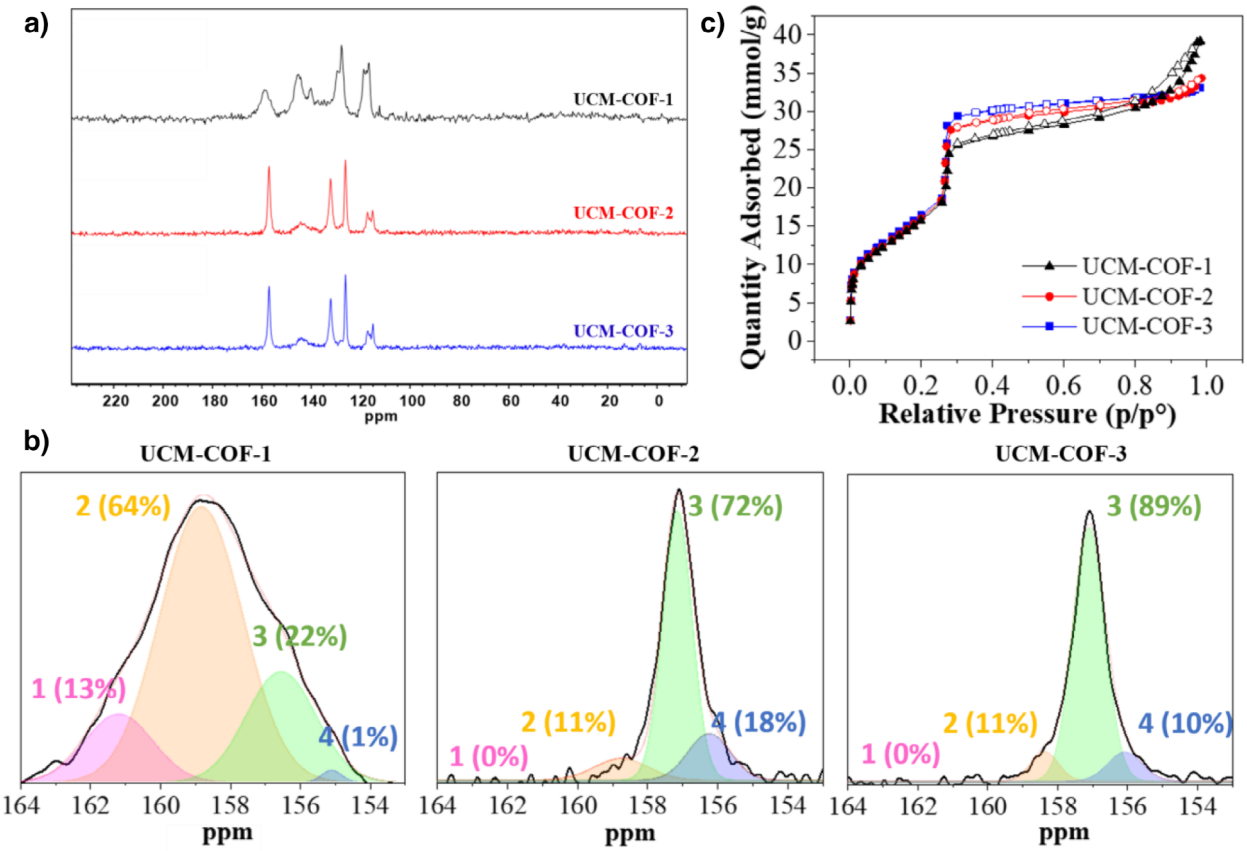

Figure 6. a) ^{13}C-CP-MAS-NMR of the UCM-COFs. b) Imine group signal area analysis signal area calculation for the different UCM-COFs. c) Nitrogen sorption isotherms at 77K (full symbols and empty symbols represent the adsorption and desorption branches, respectively).

The signal ca. −144 ppm can be assigned to the fluorine atoms of the TFTA, while the signals ca. −147, −154, and −164 ppm can be assigned to the fluorine atoms of the DFTAPB. We hypothesize that the signal ca. −154 corresponds to the linker building up the framework while the signal ca. −164 is from the terminal likers, maintaining a similar chemical shift. Through comparison of the three COFs (Figure 5c) the signals are less defined in UCM-COF-1 compared to what was observed for UCM-COF-2 and UCM-COF-3. Moreover, the signal ca. −164 seen in UCM-COF-1 disappears in UCM-COF-2 and is barely noticeable in UCM-COF-3. This can be explained through the variation in particle size of the different materials. UCM-COF-1 presents smaller sizes (vide supra) while UCM-COFs 2 and 3 present the biggest particle sizes, contributing the terminal amines nearly negligible due to a more homogenous chemical environment. Overall, the results align with ^{13}C-CP-MAS-NMR spectroscopy, obtaining more defined signals for UCM-COF-2 and UCM-COF-3 matching the different degrees of crystallinity and particle size.

The porosity of the materials was evaluated through nitrogen sorption isotherms at 77K, revealing a type IV isotherm for all the polymorphs under study, corroborating their mesoporous nature (Figure 6c). Interestingly, the pore volumes at 0.3 p/p° were calculated to be 0.89, 0.97, and 1.02 cm^2/g for UCM-COF-1, UCM-COF-2, and UCM-COF-3, respectively, which agrees with the increasing degree of crystallinity. The surface areas were calculated by using the Brunauer–Emmet–Teller model (Figures S82-84), obtaining 1209, 1196, and 1253 m^2/g, respectively, for the three materials, very close to the theoretical[18] one 1361 m^2/g, corroborating the purity of all the frameworks. Finally, the pore size distributions calculated using the nonlocal density functional theory (NLDFT) for the three polymorphs under study were centered at 3.0 nm (Figures S85-S87). Finally, the thermogravimetric analysis (TGA) for the UCM-COFs revealed negligible differences about the thermal stability of the frameworks (Figures S88-S90).

The study of the mechanical properties of COFs at the nanoscale level is typically hampered by the shape and size of the COF crystallites. However, the outstanding dimensions of UCM-COF-3 microcrystals allow us to analyze their mechanical properties by means of atomic force microscopy (AFM).

To this end, we first acquired topography images of UCM-COF-3, revealing microcrystals lying along the c-axis with an average length 2.3 ± 0.8 μm and diameter 240 ± 40 nm (Figure S91), consistent with SEM imaging. The simplest method to study mechanical properties using AFM is by performing force–distance (Fz) curves. These involve approaching the AFM tip toward the sample while recording the interaction force. In our experiments, we began by positioning the tip above one of the microcrystals (Figure 7a), with the tip initially far from the surface. The sample was then moved upward toward the tip at a constant velocity of ~1 nm/s.

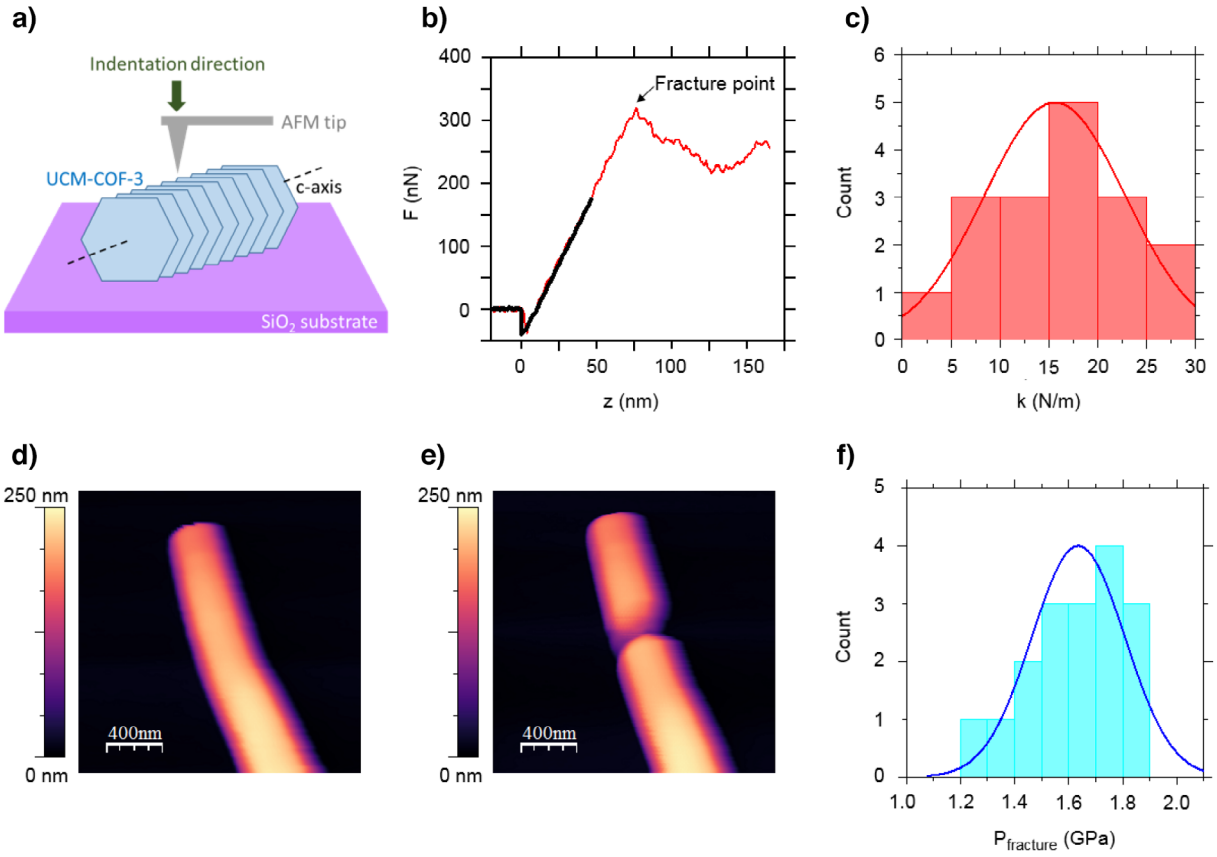

Figure 7. a) Schematic depiction of the layered structure of UCM-COF-3 crystallites and an AFM tip in a nanoindentation experiment in the direction perpendicular to the c-axis. b) Typical force (*F*) versus sample displacement (*z*) curve performed in a UCM-COF-3 single crystal in the linear and reversible deformation regime (black) and in a fracture experiment, where the force suddenly decreases after the fracture point is reached (red). c) Histogram showing the distribution of the spring constant value across different single crystals. Topographic images of a UCM-COF-3 single crystal d) before and e) after a fracture experiment, respectively. f) Histogram of the breaking strength of UCM-COF-3 single crystals.

After approximately 20 nm of approach, the tip made contact with the sample, and the cantilever began to bend, thereby applying load onto the microcrystal. We continued the approach for an additional ~150 nm, effectively performing a nanoindentation experiment. A representative loading force–distance curve obtained from one of these microcrystals exhibiting a linear elastic response, characteristic of most materials, is shown in Figure 7b. For measurements limited to the linear and reversible deformation of the single crystals, we obtained an effective spring constant in the direction perpendicular to the c-axis of $k = 16 \pm 7$ Nm^{-1} (Figure 7c). It is important to highlight that due to the layered structure of UCM-COF-3 the crystallites are highly anisotropic and thus so are its mechanical properties such as the Young's modulus.

To estimate the elastic modulus in the direction perpendicular to the c-axis *Fz* curves are not sufficient and hence we performed contact resonance atomic force microscopy (CR-AFM).[33] In brief, this technique consists of exciting the resonant modes of the AFM cantilever. When the AFM tip is not in contact with the sample, the resonant modes occur at specific frequencies that depend on the geometry of the probe. When the tip is in contact with the sample, the frequencies of the resonant modes increase due to tip-sample forces. CR-FM measures the frequencies at which the free and contact resonances occur. The Young's modulus can then be derived from these frequency shifts using appropriate models. We implemented contact resonance by performing a calibration approach that relates the resonance spectrum of the sample with a reference material of known mechanical properties.[34] From the CR-AFM measurements, we obtained an average Young Modulus of 3.78 ± 0.16 GPa in the direction perpendicular to the c-axis (Figure S92). This value is mainly related to the interlayer forces, π-π stacking, connecting the UCM-COF-3 structure and an order of magnitude higher to those values found in related imine-COF membranes[35] in which the mechanical properties are dictated by the C-H···π interactions connecting the COF grains.

When the pressure applied by the tip is further increased during the indentation experiment, a fracture of the COF single crystals is produced (Figure 7d,e). Crystal fracture is observed in the indentation curves as a sudden decrease in the applied force (Figure 7b). From these measurements, we can estimate the breaking pressure as shown in Equation 1:

$$P = \frac{1}{\pi}\left(\frac{6FE^2}{R^2}\right)^{1/3} \quad (1)$$

as given by the Hertzian contact mechanics model, where *F* is the fracture force, *E* is the Young modulus determined

in the contact resonance experiments, and R is the tip radius. We obtained an average fracture strength of 1.64 ± 0.16 GPa (Figure 7f). This high fracture strength is indicative of strong van der Waals interactions between adjacent layers, consistent with the higher exfoliation energy cost of this material when compared to its isostructural nonfluorinated COF analogue.[18]

Conclusion

Our findings highlight the critical role of TFA and F_4An in modulating the Schiff base formation and, consequently, the crystallinity of the resulting COF. The effect of carrying the reaction in the pure catalyst, in this case, TFA, yielded a new polymorph thanks to the lower solubility of the monomers in TFA and the facilitation of key proton transfer steps. We have also studied the effect of modulators, such as aniline and F_4An, on the morphology of the material, resulting in the obtainment of single crystals. In this case, F_4An is more suitable for this kind of electron-deficient system, introducing a controlled imine exchange process that slows down crystal growth, ultimately leading to higher crystallinity. Furthermore, we have observed that the effect of morphology in the material can go beyond common characterization in COFs such as PXRD, showing noticeable effects in both ^{13}C-CP-MAS-NMR and ^{19}F-CP-MAS-NMR. In addition, the mechanical response of the obtained single crystals was studied by AFM-nanoindentation. Although previous studies have reported the elastic properties of COFs assembled through covalent[36] or C─H···π interactions,[35] here we present, for the first time, a direct determination of the out-of-plane mechanical properties of a well-characterized COF single crystal. This study reveals a robust and fracture resistant material with promising properties for the development of novel COF-based advance materials such as membranes or stationary phases.

Acknowledgements

This work was financially supported by Research Project TED2021-129886B-C42, TED2021-129886B-C43, PID2022-142331NB-I00, CEX2023-001316-M granted by MCIN/AEI/10.13039/501100011033 and the European Union NextGeneration EU/ PRTR, Research Project PID2022-138908NB-C31, PID2022-138908NB-C32, PID2022-138908NB-C33 granted by MCIN/AEI/10.13039/501100011033/ and FEDER A way to make Europe. This work was also supported by the Comunidad de Madrid (TEC-2024/ECO-332) and the UCM (INV.GR.00.1819.10759). J.L.S. acknowledges the MICIIN for the REDES project "RED2022-134503-T". F.Z. also acknowledges support from the European Innovation Council under grant Agreement 101047081 (EVA). FZ acknowledges the support from the "(MAD2D-CM)-UAM" project funded by Comunidad de Madrid, by the Recovery, Transformation and Resilience Plan, and by NextGenerationEU from the European Union(The computing work is supported by USTBMatCom of Beijing Advanced Innovation Center for Materials Genome Engineering).

Conflict of Interests

The authors declare no conflict of interest.

Data Availability Statement

The data that support the findings of this study are available from the corresponding author upon reasonable request.

Keywords: AFM-indentation · COF · Mechanistic study · NRM · Single-crystal

[1] W. Zhao, Q. Zhu, X. Wu, D. Zhao, *Chem. Soc. Rev.* **2024**, *53*, 7531–7565.
[2] M. Jiménez-Duro,, E. Martínez-Periñán, M. Martínez-Fernández, J. I. Martínez, E. Lorenzo, J. L. Segura, *Small.* **2024**, *20*, 2402082.
[3] G. Valente, R. Dantas, P. Ferreira, R. Grieco, N. Patil, A. Guillem-Navajas, D. Rodríguez-San Miguel, F. Zamora, R. Guntermann, T. Bein, J. Rocha, M. H. Braga, K. Strutynski, M. Melle-Franco, R. Marcilla, M. Souto, *J. Mater. Chem. A.* **2024**, *12*, 24156–24164.
[4] Y. Liu, X. Liu, A. N. Su, C. Gong, S. Chen, L. Xia, C. Zhang, X. Tao, Y. Li, Y. Li, T. Sun, M. Bu, W. Shao, J. Zhao, X. Li, Y. Peng, P. Guo, Y. U. Han, Y. Zhu, *Chem. Soc. Rev.* **2024**, *53*, 502–544.
[5] D. Del Giudice, M. Valentini, G. Melchiorre, E. Spatola, S. Di Stefano, *Chem. - Eur. J.* **2022**, *28*, e202200685.
[6] J. Hu, S. K. Gupta, J. Ozdemir, H. Beyzavi, *ACS Appl. Nano Mater.* **2020**, *3*, 6239–6269.
[7] A. Natraj, W. Ji, J. Xin, I. Castano, D. W. Burke, A. M. Evans, M. J. Strauss, M. Ateia, L. S. Hamachi, N. C. Gianneschi, Z. A. ALOthman, J. Sun, K. Yusuf, W. R. Dichtel, *J. Am. Chem. Soc.* **2022**, *144*, 19813–19824.
[8] L. Yi, Y. Gao, S. Luo, T. Wang, H. Deng, *J. Am. Chem. Soc.* **2024**, *146*, 19643–19648.
[9] A. Natraj, I. R. Landman, C. E. Pelkowski, D. W. Burke, S. Kewalramani, W. R. Dichtel, *J. Am. Chem. Soc.* **2024**, *146*, 16775–16786.
[10] C. Kang, K. Yang, Z. Zhang, A. K. Usadi, D. C. Calabro, L. S. Baugh, Y. Wang, J. Jiang, X. Zou, Z. Huang, D. Zhao, *Nat. Commun.* **2022**, *13*, 1370.
[11] T. Ma, E. A. Kapustin, S. X. Yin, L. Liang, Z. Zhou, J. Niu, L.I.-H. Li, Y. Wang, J. Su, J. Li, X. Wang, W. D. Wang, W. Wang, J. Sun, O. M. Yaghi, *Science* **2018**, *361*, 48–52.
[12] L. Liang, Y. I. Qiu, W. D. Wang, J. Han, Y. I. Luo, W. Yu, G.-L. Yin, Z.-P. Wang, L. Zhang, J. Ni, J. Niu, J. Sun, T. Ma, W. Wang, *Angew. Chem. Int. Ed.* **2020**, *59*, 17991–17995.
[13] A. M. Evans, L. R. Parent, N. C. Flanders, R. P. Bisbey, E. Vitaku, M. S. Kirschner, R. D. Schaller, L. X. Chen, N. C. Gianneschi, W. R. Dichtel, *Science* **2018**, *361*, 52–57.
[14] L. Peng, Q. Guo, C. Song, S. Ghosh, H. Xu, L. Wang, D. Hu, L. Shi, L. Zhao, Q. Li, T. Sakurai, H. Yan, S. Seki, Y. Liu, D. Wei, *Nat. Commun.* **2021**, *12*, 5077.
[15] M. Traxler, W. R. Dichtel, *Chem. Sci.* **2024**, *15*, 7545–7551.
[16] J. Han, J. Feng, J. Kang, J.-M. Chen, X.-Y. Du, S.-Y. Ding, L. Liang, W. Wang, *Science* **2024**, *383*, 1014–1019.

[17] C. B. Whitehead, S. Özkar, R. G. Finke, *Chem. Mater.* **2019**, *31*, 7116–7132.
[18] M. Martínez-Fernández, E. Martínez-Periñán, A. de la Peña Ruigómez, J. J. Cabrera-Trujillo, J. A. R. Navarro, F. Aguilar-Galindo, D. Rodríguez-San-Miguel, M. Ramos, R. Vismara, F. Zamora, E. Lorenzo, J. L. Segura, *Angew. Chem. Int. Ed.* **2023**, *62*, e202313940.
[19] S. Kandambeth, V. Venkatesh, D. B. Shinde, S. Kumari, A. Halder, S. Verma, R. Banerjee, *Nat. Commun.* **2015**, *6*, 6786.
[20] H. S. Sasmal, A. Kumar Mahato, P. Majumder, R. Banerjee, *J. Am. Chem. Soc.* **2022**, *144*, 11482–11498.
[21] H. Zhao, G. Liu, Y. Liu, L. Zhou, L. Ma, Y. He, X. Zheng, J. Gao, Y. Jiang, *Nano Res.* **2023**, *16*, 281–289.
[22] Z. Xiong, B. Sun, H. Zou, R. Wang, Q. Fang, Z. Zhang, S. Qiu, *J. Am. Chem. Soc.* **2022**, *144*, 6583–6593.
[23] B. J. Smith, W. R. Dichtel, *J. Am. Chem. Soc.* **2014**, *136*, 8783–8789.
[24] J. Sprachmann, N. Grabicki, A. Möckel, J. Maltitz, J. R. Monroy, G. J. Smales, O. Dumele, *Chem. Commun.* **2023**, *59*, 13639–13642.
[25] B. H. Toby, R. B. Von Dreele, *J. Appl. Crystallogr.* **2013**, *46*, 544–549.
[26] J. H. Toby, R. B. Von Dreele, M. K. Y. Chan, B. H. Toby, *J. Appl. Crystallogr.* **2018**, *51*, 1244–50.
[27] W. F. Hosford, *In Materials Science: An Intermediate Text*, Cambridge University Press, Cambridge, **2006**, pp. 21–25.
[28] J. Schindelin, C. T. Rueden, M. C. Hiner, K. W. Eliceiri, *Mol. Reprod. Dev.* **2015**, *82*, 518–529.
[29] Y. Ding, Y. Cui, T. Li, *J. Phys. Chem.A* **2015**, *119*, 4252–4260.
[30] P. J. Silva, *PeerJ Org. Chem.* **2020**, *2*, e4.
[31] C. Solís-Calero, J. Ortega-Castro, A. Hernández-Laguna, F. Muñoz, *Theor. Chem. Acc.* **2012**, *131*, 1263.
[32] C. Kang, Z. Zhang, A. K. Usadi, D. C. Calabro, L. S. Baugh, K. Yu, Y. Wang, D. Zhao, *J. Am. Chem. Soc.* **2022**, *144*, 3192–3199.
[33] G. Stan, S. Krylyuk, A. V. Davydov, M. D. Vaudin, L. A. Bendersky, R. F. Cook, *Ultramicroscopy* **2009**, *109*, 929–936.
[34] B. Bhushan, H. Fuchs, *Applied Scanning Probe Methods XI*, eds. B. Bhushan, H. Fuchs, (Springer-Verlag, Berlin Heidelberg New York) Chapter *5*, pp. 97–138.
[35] J. Á. Martín-Illán, J. A. Suárez, J. Gómez-Herrero, P. Ares, D. Gallego-Fuente, Y. Cheng, D. Zhao, D. Maspoch, F. Zamora, *Adv. Sci.* **2022**, *9*, 21046430.
[36] Q. Fang, Z. Pang, Q. Ai, Y. Liu, T. Zhai, D. Steinbach, G. Gao, Y. Zhu, T. Li, J. Lou, *Proc. Natl. Ac. Sci.* **2023**, *120*, e2208676120.

Manuscript received: May 11, 2025
Revised manuscript received: July 15, 2025
Accepted manuscript online: July 16, 2025
Version of record online: ■■, ■■

Research Article

Organic Materials

M. Jiménez-Duro, M. Martínez-Fernández*, J. J. Cabrera-Trujillo, E. Osuna, M. F.-R. Humanes, C. Gómez-Navarro, J. Gómez-Herrero, F. Zamora, J. L. Segura* ——— **e202510312**

Unconventional Fast Room Temperature Synthesis of Covalent Organic Framework Single Crystals Unveiling Precise Structural Insights

This work presents a fast, room-temperature synthesis of single-crystalline, highly fluorinated 2D covalent organic frameworks (COFs). We achieved the growth of 3-micron-long COF rods, enabling the precise study of their mechanical properties and aggregation states. The crystallization process was computationally elucidated, revealing the critical roles of trifluoroacetic acid and 2,3,5,6-tetrafluoroaniline in promoting Schiff base bond formation and improving COF crystallinity. This study offers new insights into the controlled synthesis of 2D COFs, with implications for their use in a range of advanced materials applications.